



## Two-phase interface in $\text{LiMnPO}_4$ nanoplates

Youzhong Dong<sup>a,b</sup>, Long Wang<sup>b</sup>, Shouliang Zhang<sup>b</sup>, Yanming Zhao<sup>a</sup>, Jiping Zhou<sup>b</sup>, Hui Xie<sup>b</sup>, John B. Goodenough<sup>b,\*</sup>

<sup>a</sup> Department of Physics, South China University of Technology, Guangzhou 510641, PR China

<sup>b</sup> Texas Materials Institute and the Materials Science and Engineering Program, The University of Texas at Austin, 204 E Dean Keeton st stop C2201, ETC 9.184, Austin, TX 78712, United States

### HIGHLIGHTS

- Synthesis and orientation of  $\text{LiMnPO}_4$  nanoplatelets.
- Orientation of  $\text{MnPO}_4/\text{LiMnPO}_4$  two-phase interface versus 1D Li-diffusion channels.
- Strain across and mobility of the  $\text{MnPO}_4/\text{LiMnPO}_4$  two-phase boundary in  $\text{Li}_{1-x}\text{MnPO}_4$ .

### ARTICLE INFO

#### Article history:

Received 22 February 2012

Received in revised form

13 March 2012

Accepted 15 March 2012

Available online 7 May 2012

#### Keywords:

Li-ion batteries

Olivines

$\text{Li}^+$  diffusion

Jahn-Teller distortion

### ABSTRACT

The poor electrochemical performance of  $\text{LiMnPO}_4$  nanoplates relative to that of isostructural  $\text{LiFePO}_4$  is clarified.  $\text{LiMnPO}_4$  nanoplates *ca.* 2 nm in diameter and 50 nm thick were prepared by a single solvothermal method. The [010] 1D  $\text{Li}^+$  diffusion path lies in the plane of the platelets, and the two-phase  $\text{LiMnPO}_4/\text{MnPO}_4$  interface intersects the [010] direction. A 10% volume change and a cooperative Jahn-Teller distortion of the  $\text{Mn}^{3+}$  sites in the  $\text{MnPO}_4$  phase introduces a large strain across the interface that impedes the rate of interface motion and therefore the rate of Li extraction/insertion. Nevertheless, a capacity of  $107.5 \text{ mAh g}^{-1}$  at the C/20 rate had a capacity fade of only 0.08% per cycle  $\text{LiFePO}_4$  platelets, on the other hand, have the [010] 1D  $\text{Li}^+$  diffusion paths perpendicular to the platelets and the  $\text{LiFePO}_4$  interface parallel to the [010] direction, which leaves short diffusion lengths that are not blocked by structural changes.

© 2012 Elsevier B.V. All rights reserved.

## 1. Introduction

The electrochemical performance of lithium-ion batteries is largely determined by the cathode materials, which require fast lithium-ion diffusion over a large solid-solution range during the charge/discharge process [1–3].  $\text{LiMPO}_4$  ( $\text{M} = \text{Mn, Fe, Co, Ni}$ ) materials with the ordered-olivine structure are known to have an adequate solid-solution range for use as rechargeable cathodes. Among them,  $\text{LiMnPO}_4$  is considered to exhibit the best potential,  $\sim 4.1 \text{ V vs. Li}^+/\text{Li}$ , for matching the HOMO of the organic liquid-carbonate electrolytes that are presently used in Li rechargeable batteries; it is also low in cost [4]. Hence,  $\text{LiMnPO}_4$  would be an ideal substitute for the commonly used cathode materials.

However,  $\text{LiMnPO}_4$  suffers from low electronic conductivity ( $< 10^{-10} \text{ S cm}^{-1}$ ) leading to lower capacity and limited rate

capability [5,6]. In addition, the appearance of a Jahn–Teller distortion is predicted to create a large kinetic barrier to ion and electron hopping at the mismatched  $\text{MnPO}_4/\text{LiMnPO}_4$  interface [7]. There have been many efforts in recent years to increase the electronic conductivity of  $\text{LiMnPO}_4$  by cationic doping, decreasing the particle size, or coating with electronically conducting agents [8–10]. Nanostructured materials provide short diffusion lengths for both  $\text{Li}^+$ -ion diffusion and electron transport, which can enhance charge/discharge rates [11]. Several procedures for the synthesis of nanostructured  $\text{LiMnPO}_4$  have been reported; they include the hydrothermal process [12], ultrasonic spray pyrolysis [13], the polyol process [14] and solvothermal methods [15]. Although the nanometer-sized materials can improve the electrochemical performance to a certain extent, the morphology of the olivine particles is a critical factor that determines the rate of  $\text{Li}^+$  extraction/insertion.

The  $\text{Li}^+$  ions move in 1D *b*-axis channels in the ordered-olivine structure in the orthorhombic space group *Pnma* [16–18]. However, Amin et al. claim [19], from transport measurements on single-

\* Corresponding author. Tel.: +1 512 471 1646; fax: +1 512 471 7681.  
E-mail address: [jgoodenough@mail.utexas.edu](mailto:jgoodenough@mail.utexas.edu) (J.B. Goodenough).

crystal  $\text{LiFePO}_4$ , that electronic conductivity, ionic conductivity, and chemical diffusivity of Li are all found to be essentially two-dimensional with similar components in  $b$  and  $c$  directions. Moreover, Choi et al. have shown that  $\text{LiMnPO}_4$  nanoplates with a (100) face perpendicular to the  $a$ -axis gives a respectable electrochemical performance [20].

In the present study, we report the synthesis and electrochemical performance of  $\text{LiMnPO}_4$  nanoplates prepared by a simple solvothermal method. The short dimension of the  $\text{LiMnPO}_4$  nanoplates was determined by XRD and TEM. Although the  $b$ -axis parallel to the short dimension is more favorable for an olivine cathode, the  $\text{LiMnPO}_4$  nanoplates have their short direction along the  $a$ -axis. Nevertheless, nanoparticles show an interesting electrochemical performance. In addition, we provide direct experimental evidence for the appearance of a Jahn–Teller distortion in  $\text{MnPO}_4$  that raises the kinetic barrier at the mismatched  $\text{MnPO}_4/\text{LiMnPO}_4$  interface. Moreover the two-phase interface is not parallel to the  $b$ -axis in the (100) plane, but intersects it, which makes it more difficult to move the interface.

## 2. Experimental

The  $\text{LiMnPO}_4$  nanoplates were synthesized by a solvothermal method. Lithium dihydrogen phosphate ( $\text{LiH}_2\text{PO}_4$ , Aldrich) and Manganese acetate tetrahydrate ( $\text{C}_4\text{H}_6\text{MnO}_4 \cdot 4\text{H}_2\text{O}$ , Alfa Aesar) with the molar ratio of 1:1 were used as the precursors. First, a reddish, transparent precursor solution was prepared by dissolving the appropriate amount of  $\text{C}_4\text{H}_6\text{MnO}_4 \cdot 4\text{H}_2\text{O}$  in 35 ml ethylene glycol under constant stirring at room temperature for 30 min. Then, the required amount of  $\text{LiH}_2\text{PO}_4$  was slowly added to the above solution under constant stirring for 60 min. The obtained solution was transferred into a Teflon vessel and sealed tightly in a stainless-steel autoclave. The autoclave was heated to 200 °C for 12 h in an oven and then allowed to cool down to ambient temperature. The precipitated products were filtrated, washed several times with ethanol, and finally dried at 120 °C for 10 h. To obtain the  $\text{LiMnPO}_4$  particles, the Lithium dihydrogen phosphate and Manganese acetate tetrahydrate with the molar ratio of 1:1 were ground in an agate mortar and heated at 600 °C for 4 h under a stream of reducing atmosphere (95%Ar + 5%H<sub>2</sub>) in a quartz tube furnace.

The chemical extraction of lithium in non-aqueous medium was carried out at room temperature by stirring the  $\text{LiMnPO}_4$  sample in

an acetonitrile solution of  $\text{NO}_2\text{BF}_4$  for 24 h in an argon filled glove box. The products formed after the reaction were washed three times with acetonitrile under argon atmosphere to remove  $\text{LiBF}_4$  and dried under vacuum at ambient temperature.

Powder X-ray diffraction (XRD) patterns of the products were recorded at room temperature with a Philips X-ray diffractometer equipped with  $\text{Cu K}\alpha$  radiation in a step-scanning mode over the range 10–90° with a step width of 0.02° and a step time of 5 s.

Scanning electron microscopy (SEM) was performed with a JEOL JSM-5610 and FEI Strata™ DB235 SEM/FIB microscope. The high-resolution transmission electron microscopy (HRTEM) images and selected-area electron diffraction (SAED) patterns were carried out on a transmission electron microscope (JEOL 2010F).

The Electrochemical performances of the samples were evaluated with a standard CR2032 coin cell. The electrodes containing the  $\text{LiMnPO}_4$  were prepared by the following procedure: Solvothermally synthesized  $\text{LiMnPO}_4$  and glucose in the weight ratio 1:1 were ground and heated to 500 °C for 2 h in Ar/H<sub>2</sub> (95:5) to

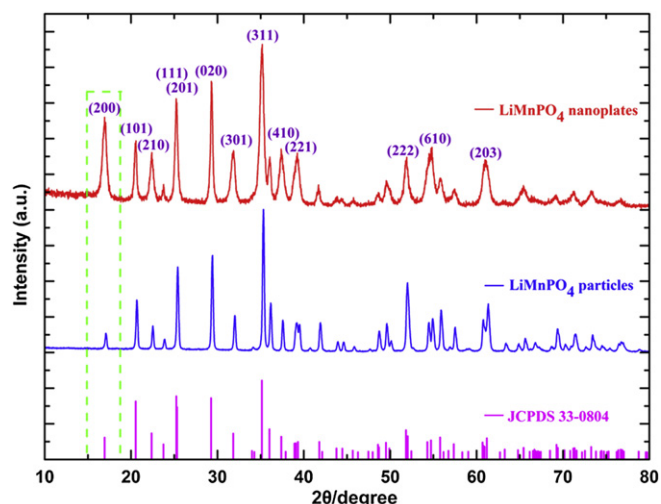


Fig. 1. The XRD pattern of the  $\text{LiMnPO}_4$  nanoplates and  $\text{LiMnPO}_4$  particles.

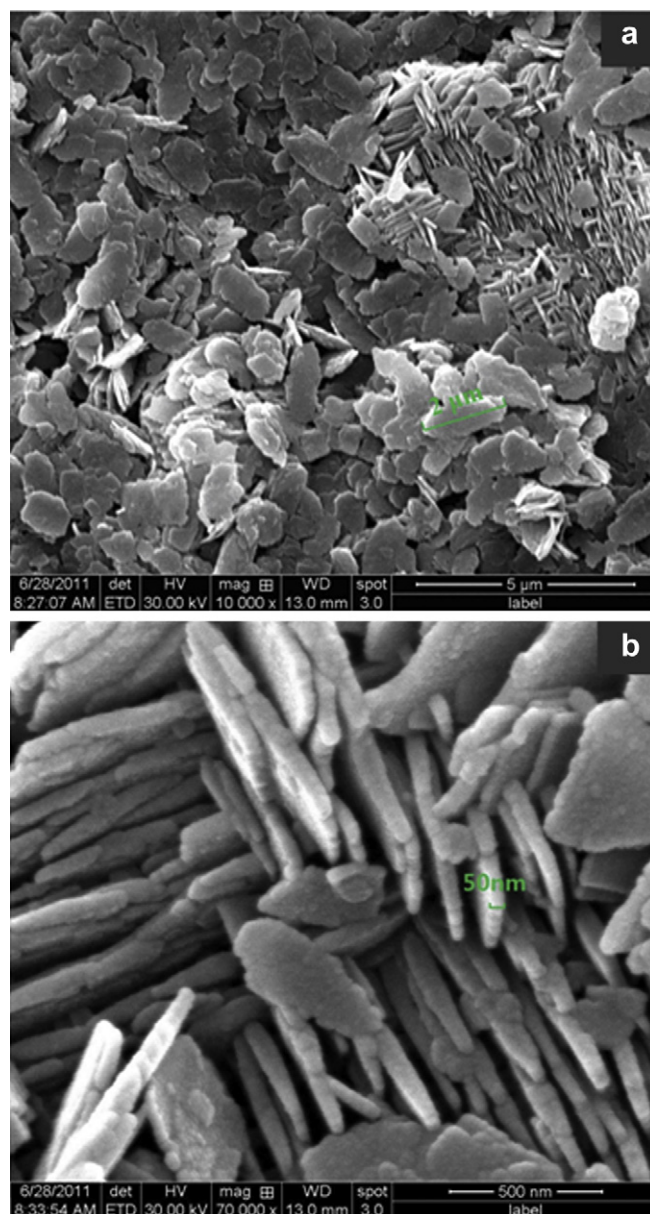


Fig. 2. The SEM images of the  $\text{LiMnPO}_4$  nanoplates with different magnification: (a) Representative SEM images, (b) High-magnification SEM images.

obtain a carbon-coated  $\text{LiMnPO}_4$  ( $\text{LiMnPO}_4/\text{C}$ ) composite; 12% wt.% Carbon was found on  $\text{LiMnPO}_4/\text{C}$  from thermogravimetric analysis. The cathode was prepared by mixing  $\text{LiMnPO}_4/\text{C}$  with acetylene black (Alfa Aesar) and polytetrafluoroethylene (PTFE) binder (G163, AGC company) with a weight ratio of 75:20:5; the mixture was rolled into thin sheets that were punched into circular discs 0.78 cm in diameter. The punched electrodes were dried in a vacuum oven at 120 °C overnight before assembling the coin cells. Half-cells with a polypropylene membrane separator, Li metal as the anode and the reference in 1 M  $\text{LiPF}_6$  in ethylene carbonate/dimethyl carbonate (EC/DMC) (1:1 v/v) electrolyte were assembled in a glove box filled with ultrahigh-purity argon. The electrochemical performance of the  $\text{LiMnPO}_4$  nanoplates was evaluated with an Arbin Instruments testing system (Arbin BT-2000) at room temperature and the electrochemical capacity of samples was evaluated based only on the active material weight.

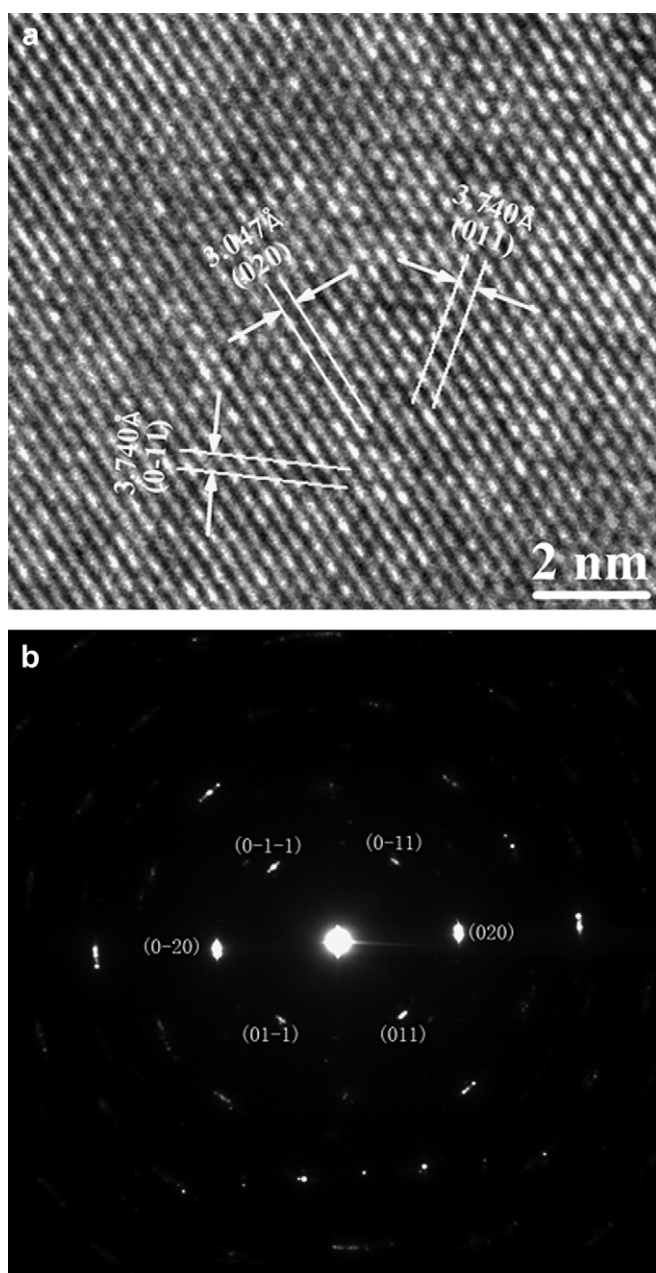


Fig. 3. (a) The HRTEM images and (b) the SAED pattern of the  $\text{LiMnPO}_4$  nanoplate.

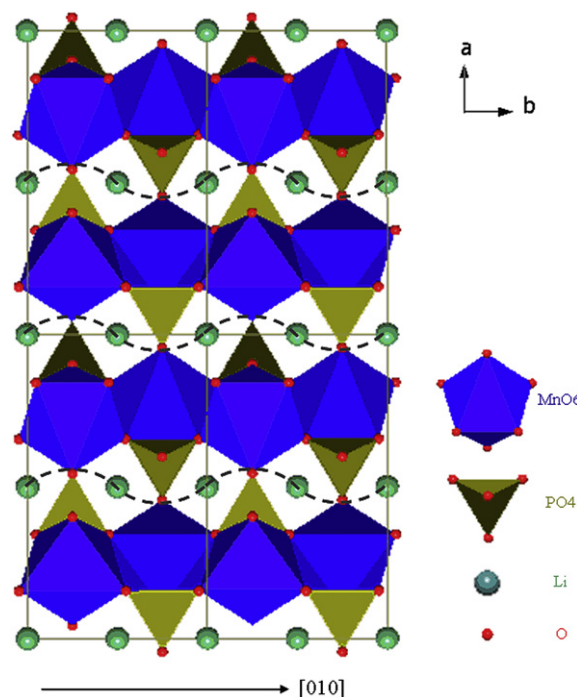


Fig. 4. The Schematic diagram of  $\text{Li}^+$  transportation in  $\text{LiMnPO}_4$  compound.

### 3. Results and discussion

The crystal structure of the  $\text{LiMnPO}_4$  nanoplates was studied by powder XRD (Fig. 1). For comparison, the XRD pattern of the  $\text{LiMnPO}_4$  particles and the position and the relative intensity of the peaks of a crystalline  $\text{LiMnPO}_4$  sample (JCPDS card No. 33-0804) are shown in the same figure. The result shows that the nanoplates are single-phase  $\text{LiMnPO}_4$  with the orthorhombic olivine structure. It is interesting that the  $\text{LiMnPO}_4$  nanoplates yield XRD reflections with relative intensity homologous to those produced by  $\text{LiMnPO}_4$  particles, as obtained from JCPDS card No. 33-0804, except for the (200) reflection. In contrast, the relative intensity of the 200 reflection was increased several times in the XRD pattern of the  $\text{LiMnPO}_4$  nanoplates. The markedly increased (200) reflection in

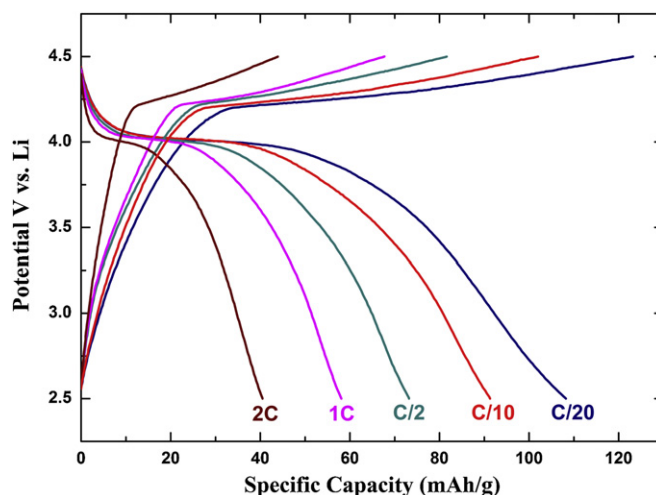


Fig. 5. Typical voltage profiles of the  $\text{LiMnPO}_4$  nanoplates at various charge/discharge rates (C/20, C/10, C/2, 1C and 2C) at room temperature.



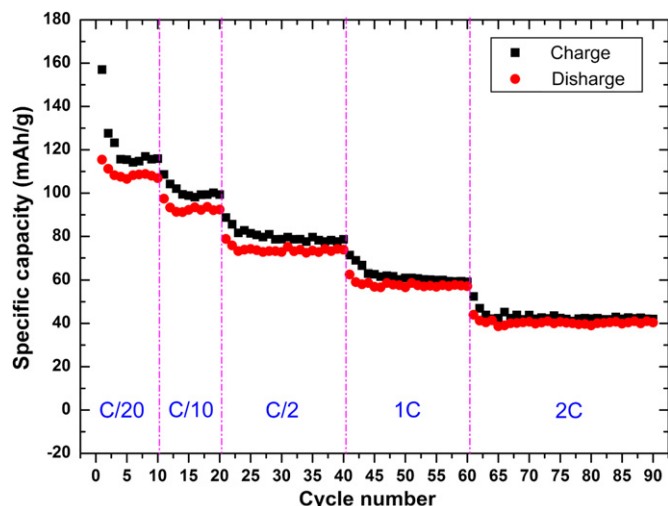


Fig. 6. The cycle performance of the LiMnPO<sub>4</sub> nanoplates at different charge/discharge rates (C/20, C/10, C/2, 1C and 2C) at room temperature.

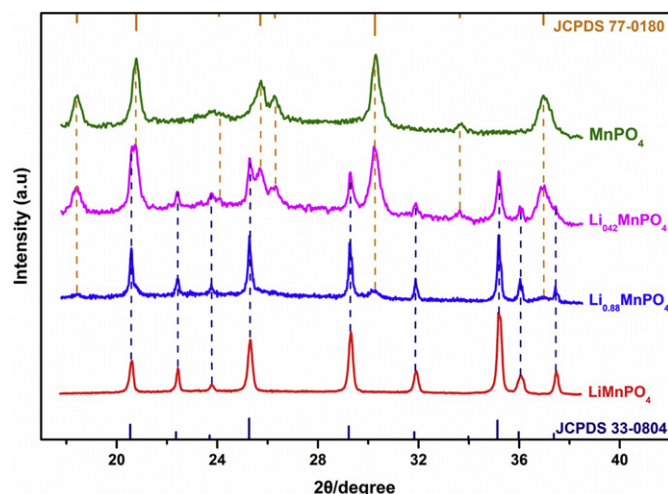


Fig. 7. XRD patterns of a series of Li<sub>x</sub>MnPO<sub>4</sub> compositions ( $0 \leq x \leq 1$ ), prepared by chemical delithiation of LiMnPO<sub>4</sub>.

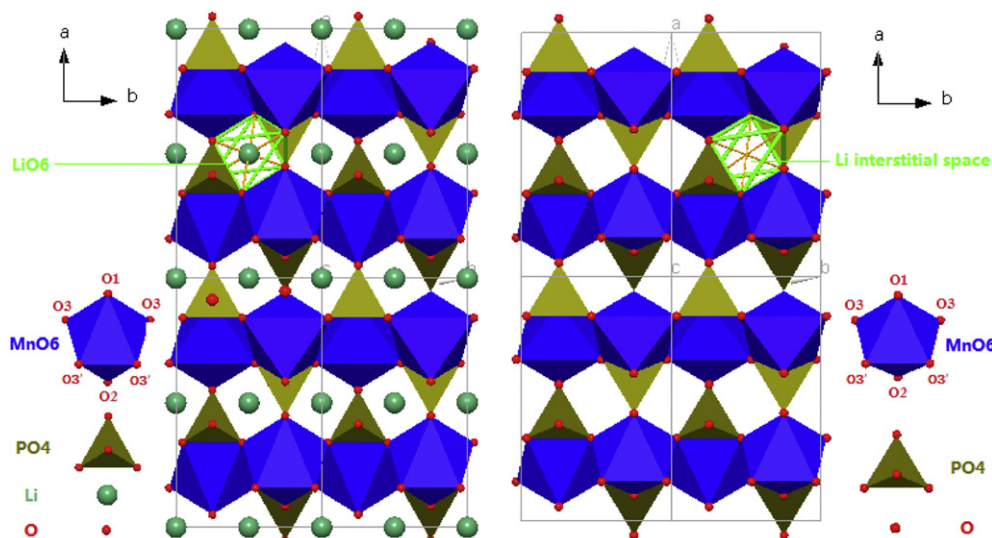


Fig. 8. The structure of the LiMnPO<sub>4</sub> and the MnPO<sub>4</sub> samples.

the XRD pattern indicates that the LiMnPO<sub>4</sub> nanoplates have a (100) face. Fig. 2 shows the SEM image of LiMnPO<sub>4</sub> nanoplates with a diameter of around 2  $\mu\text{m}$  and a thickness of around 50 nm.

In order to confirm the preferred direction, the crystallographic orientation of the LiMnPO<sub>4</sub> nanoplates was analyzed with TEM. Fig. 3 shows the HRTEM images and SAED pattern of the LiMnPO<sub>4</sub> nanoplates. The interplanar spacing of 3.047 Å and 3.740 Å in Fig. 3a can be identified as the (020) and (011) lattice planes, respectively, indicating that the crystallographic face of the nanoplates is the (100) plane. The corresponding SAED pattern also indicates the (100) plane is the plane face as well as the single-crystal nature of the LiMnPO<sub>4</sub> nanoplates.

In the ordered-olivine structure of LiMnPO<sub>4</sub>, like that of LiFePO<sub>4</sub>, Li<sup>+</sup> transport follows a zigzag one-dimensional pathway along the *b* direction (Fig. 4). LiMnPO<sub>4</sub> nanoplates with a face perpendicular to the (100) direction have a short length that is parallel to the *a* axis, which is not electrochemically active for Li<sup>+</sup> transport. In contrast, with (010) planes as the plate face in LiFePO<sub>4</sub>, the short length is the most active *b* axis for Li<sup>+</sup> deintercalation/intercalation. If a LiMnPO<sub>4</sub> nanoplate were to grow with a short length perpendicular to the (010) direction, the rate capability of batteries employing LiMnPO<sub>4</sub> nanoplates as cathode materials could be significantly improved. Nevertheless, Choi et al. [20] have also shown that the LiMnPO<sub>4</sub> nanoplates with the *b* axis in the plates can give an interesting electrochemical performance.

Fig. 5 presents typical voltage profiles of our LiMnPO<sub>4</sub> nanoplates at various charge/discharge rates between C/20 and 2C in the voltage range between 2.5 and 4.5 V. Similar to the results of Choi et al. [20], the voltage profiles clearly show a flat redox potential around 4.1 V vs. Li/Li<sup>+</sup> at low rates, indicating that the charge/discharge reaction proceeds via a first-order phase transition between LiMnPO<sub>4</sub> and MnPO<sub>4</sub>. Although the LiMnPO<sub>4</sub> nanoplates have the *b* axis within the particle plates, a high specific capacity of 108.2 mAh g<sup>-1</sup> was still achieved at C/20; even at a 2C rate, a specific capacity of 40.5 mAh g<sup>-1</sup> was delivered. The capacity decrease with increasing discharge rates is consistent with primary Li<sup>+</sup>-ion diffusion within the (100) planes.

The cycle performance of the LiMnPO<sub>4</sub> nanoplates is given in Fig. 6. In order to investigate the rate capability during cycling, various current rates of C/20, C/10, C/2, 1C and 2C were applied to the working electrode. Except for the first three cycles, the sample shows a relatively stable charge/discharge capacity. Even at the 2C rate, the capacity fade was only 0.09% per cycle. The difference

**Table 1**  
The structure parameters of the LiMnPO<sub>4</sub> and the MnPO<sub>4</sub> samples.

(a) LiMnPO <sub>4</sub>	(b) MnPO <sub>4</sub>
Space group: <i>Pnma</i> (orthorhombic)	Space group: <i>Pnma</i> (orthorhombic)
Unit cell parameters:	Unit cell parameters:
<i>a</i> = 10.4522(15) Å	<i>a</i> = 9.6469(19) Å
<i>b</i> = 6.1054(7) Å	<i>b</i> = 5.9178(23) Å
<i>c</i> = 4.7453(9) Å	<i>c</i> = 4.7814(8) Å
Cell volume: 302.82 Å <sup>3</sup>	Cell volume: 272.96 Å <sup>3</sup>
Mn–O Interatomic distances (Å)	Mn–O Interatomic distances (Å)
Mn–O1 2.2252(4)	Mn–O1 1.9647(2)
Mn–O2 2.2298(3)	Mn–O2 1.9319(1)
Mn–O3 2.1817(4)	Mn–O3 1.9402(2)
Mn–O3 2.1817(4)	Mn–O3 1.9402(2)
Mn–O3' 2.2054(2)	Mn–O3' 2.3557(3)
Mn–O3' 2.2054(2)	Mn–O3' 2.3557(3)

between the charge and discharge capacities, which represents an irreversible loss, decreases with cycling, which is why it is smaller at 2C in Fig. 6 than at C/20 rate. A similar phenomenon has been reported by Choi et al. [20], who achieved a capacity of 168 mAh g<sup>−1</sup> at C/25 rate with smaller, thinner particles. The origin of this initial irreversible capacity loss has not been determined.

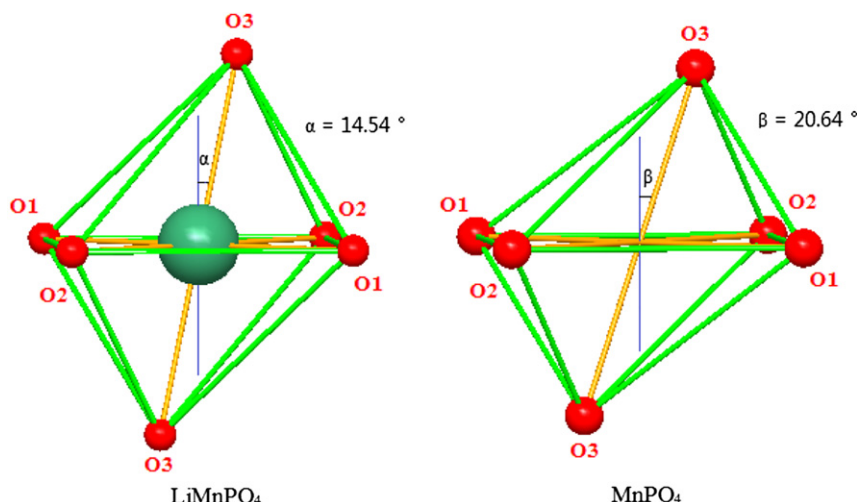
In order to understand the reason for the poor rate capability, a series of Li<sub>x</sub>MnPO<sub>4</sub> compositions (0 ≤ *x* ≤ 1) were prepared by chemical delithiation of LiMnPO<sub>4</sub> with *x* being controlled by the initial stoichiometry of NO<sub>2</sub>BF<sub>4</sub> in the solution. The corresponding XRD patterns are shown in Fig. 7. For comparison, the same figure shows the position and the relative intensity of the peaks of a crystalline LiMnPO<sub>4</sub> sample (JCPDS card no. 33-0804) and MnPO<sub>4</sub> sample (JCPDS card no. 77-0180) at the bottom and the top, respectively. According to the Laffont et al. experimental method [21], values of *x* were deduced from calibration curves of the *I*<sub>LiMnPO<sub>4</sub></sub> : (*I*<sub>LiMnPO<sub>4</sub></sub> + *I*<sub>MnPO<sub>4</sub></sub>) ratios of the intensities of both (200) and (210) reflections established from XRD patterns of *x*LiMnPO<sub>4</sub> + (1 − *x*)MnPO<sub>4</sub> mixtures (prepared by simply mixing LiMnPO<sub>4</sub> and MnPO<sub>4</sub> powders in a mortar). Integrations and decompositions of the diffraction peaks were made with the Full-Prof Suite. For Li<sub>x</sub>MnPO<sub>4</sub>, the compositions were two-phase.

Like LiFePO<sub>4</sub>, the extraction of lithium from LiMnPO<sub>4</sub> is accompanied by a direct transition to MnPO<sub>4</sub> that leaves the olivine MnPO<sub>4</sub> framework intact. Fig. 8 shows the structures of LiMnPO<sub>4</sub> and MnPO<sub>4</sub>. The corresponding structure parameters

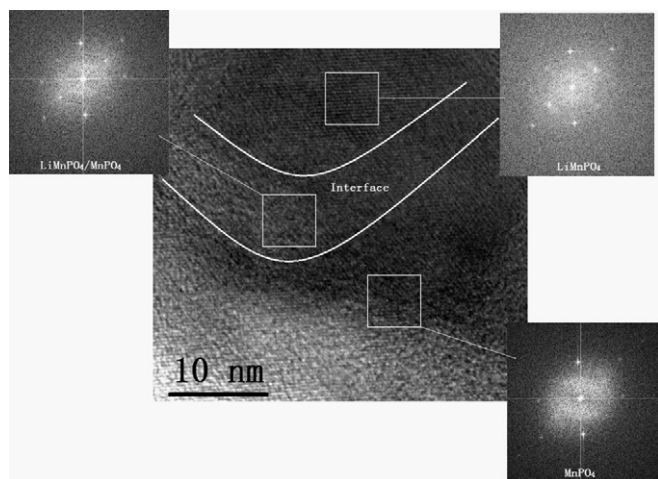
are listed in Table 1. Although the crystal structure did not change significantly from LiMnPO<sub>4</sub> to MnPO<sub>4</sub>, the unit-cell parameters and Mn–O bond lengths did change. The unit-cell parameters *a* and *b* of the LiMnPO<sub>4</sub> phase are 10.4522 Å and 6.1054 Å, respectively; the MnPO<sub>4</sub> values are 9.6469 Å and 5.9178 Å, respectively. The cell volume changes from 302.82 Å<sup>3</sup> for LiMnPO<sub>4</sub> to 272.96 Å<sup>3</sup> for MnPO<sub>4</sub>; the volume contraction of about 10% is larger than the 6.8% for LiFePO<sub>4</sub> [22]. In addition, Mn<sup>3+</sup>O<sub>6</sub> octahedra become severely distorted by orbital order on, the Mn<sup>3+</sup> ions; the Mn<sup>3+</sup>–O3' bonds are elongated, the Mn<sup>3+</sup>–O1, Mn<sup>3+</sup>–O2 and Mn<sup>3+</sup>–O3 bond lengths are shortened. Normally, the Jahn–Teller distortion of a Mn<sup>3+</sup>O<sub>6</sub> octahedron shows an elongation of the two axial bond lengths and shrinkage of the four equatorial bond lengths to give a tetragonal *c/a* > 1 site distortion. However, in LiMnPO<sub>4</sub>, the strong bonding within the (PO<sub>4</sub>)<sup>3−</sup> complexes forces a shorter O3'–O3' separation of the edge shared with a (PO<sub>4</sub>)<sup>3−</sup> relative to the O3–O3 separation sharing only corners (see Table 1). As a result, the Mn<sup>2+</sup> ion of LiMnPO<sub>4</sub> displaced toward the O3–O3 edge. On removal of Li, this displacement biases the Jahn–Teller orbital order on the Mn<sup>3+</sup> ions toward an empty axial (O1–Mn<sup>3+</sup>–O2) 3<sub>z</sub><sup>2</sup> − *r*<sup>2</sup> orbital, i.e. a *c/a* < 1 distortion, as can be seen in Table 1 by the shortening of the mean axial Mn–O1 and Mn–O2 bonds relative to the mean Mn–O3, O3' bonds; there is a stronger shift of the Mn<sup>3+</sup> ions from the O3'–O3' edge toward the O3–O3 edge that is induced by the coulomb Mn–P coulomb repulsion as well as the strong bonding in the (PO<sub>4</sub>)<sup>3−</sup> ions.

Fig. 9 shows the distorted interstitial octahedron of the MnPO<sub>4</sub> framework that is occupied by Li<sup>+</sup> in LiMnPO<sub>4</sub> and is empty in MnPO<sub>4</sub>. Although the volume of the two octahedra are similar, 11.86 versus 11.42 Å<sup>3</sup> for LiMnPO<sub>4</sub> versus MnPO<sub>4</sub>, the site distortion is increase in MnPO<sub>4</sub>; the tilt angle α = 14.54° of the O3–O3 axis from the O1–O1 axis in LiMnPO<sub>4</sub> increases to β = 20.64° in MnPO<sub>4</sub>.

In order to observe directly the two-phase MnPO<sub>4</sub>/LiMnPO<sub>4</sub> interface, we have imaged a partially delithiated Li<sub>0.42</sub>MnPO<sub>4</sub> nanoplate with HRTEM; Fig. 10 shows the Fourier transforms of the MnPO<sub>4</sub> region located at the edge of the sample, the LiMnPO<sub>4</sub> region located in the center of the sample, and the interface region between them. The Fourier transforms of the interface region is composed of diffraction spots from both phases. The volume difference between the two phases creates a large strain at the interface, which increases the activation energy for Li<sup>+</sup> insertion/extraction and lowers the rate of Li<sup>+</sup> diffusion.



**Fig. 9.** An interstitial octahedral site of the MnPO<sub>4</sub> framework that is occupied by Li<sup>+</sup> in LiMnPO<sub>4</sub> and is empty in MnPO<sub>4</sub>.



**Fig. 10.** HRTEM imaging of the chemically delithiated sample of  $\text{Li}_{0.42}\text{MnPO}_4$  with the Fourier transforms of the indicated areas.

In  $\text{LiFePO}_4$ , where the  $[010]$  axis is perpendicular to a plate, the interface boundary is parallel to the direction of motion of the  $\text{Li}^+$  ions whereas in  $\text{LiMnPO}_4$  the interface intersects the  $[101]$  axis to impede  $\text{Li}^+$  diffusion.

#### 4. Conclusion

$\text{LiMnPO}_4$  nanoplates with the orthorhombic ordered-olivine structure were prepared by a simple solvothermal method. The  $\text{LiMnPO}_4$  nanoplates have a diameter around  $2\ \mu\text{m}$  and a thickness of around  $50\ \text{nm}$ . HRTEM images and SAED patterns of the  $\text{LiMnPO}_4$  nanoplates indicate that the crystallographic face of the nanoplates is the  $(100)$  plane, which agrees with deduction from the XRD pattern. Although the  $\text{LiMnPO}_4$  nanoplates with a  $(100)$  plane have 1D  $[010]$   $\text{Li}^+$  diffusion in the plane, nevertheless the  $\text{LiMnPO}_4$  nanoplates have a significant capacity and relatively stable charge/discharge capacities. Except for the first three cycles, the discharge of the sample is  $107.5\ \text{mAh g}^{-1}$  at the rate of  $C/20$ , and the mean capacity fade is  $0.08\%$  per cycle. During the extraction/reinsertion of lithium, the olivine unit-cell volume changed from  $302.82\ \text{\AA}^3$  for  $\text{LiMnPO}_4$  to  $272.96\ \text{\AA}^3$  for  $\text{MnPO}_4$ ; the volume contraction of about  $10\%$  is larger than the  $6.8\%$  for  $\text{LiFePO}_4$ . More significant is orientation of the two-phases interface relative to the 1D  $\text{Li}^+$  diffusion path. The nanoplates permitted HREM imaging of the  $\text{MnPO}_4$ /

$\text{LiMnPO}_4$  interface intersecting the  $[010]$   $\text{Li}^+$ -diffusion axis in the  $(100)$  plane. This geometry impedes the  $\text{Li}^+$  diffusion rate because of the large lattice strains that must accompany the  $\text{Li}^+$  diffusion. In  $\text{LiFePO}_4$ , the  $\text{FePO}_4/\text{LiFePO}_4$  interface is parallel to the  $\text{Li}^+$  diffusion pathway, which is perpendicular to the  $\text{LiFePO}_4$  platelets. The parallel interface is more easily moved by fast insertion/extraction of  $\text{Li}^+$  parallel to the interface.

#### Acknowledgements

This work was supported by the Assistant Secretary for Energy Efficiency and Renewable Energy, Office of Vehicle Technologies, U.S. Department of Energy, under Contract DE-AC02-05CH11231 through the Batteries for Advanced Transportation Technologies (BATT) Program Subcontract 6805919. The work was also supported by the Office of Basic Energy Sciences Office of Science, U.S. Department of Energy, under Contract DESC0005397.

#### References

- [1] K.M. Abraham, D.M. Pasquariello, E.M. Willstaedt, *J. Electrochem. Soc.* 145 (1998) 482.
- [2] K. Kang, Y.S. Meng, J. Br  ger, C.P. Grey, G. Ceder, *Science* 113 (2006) 977.
- [3] S.B. Schougaard, J. Br  ger, M. Jiang, C.P. Grey, J.B. Goodenough, *Adv. Mater.* 18 (2006) 905.
- [4] A.K. Padhi, K.S. Nanjundaswamy, J.B. Goodenough, *J. Electrochem. Soc.* 144 (1997) 188.
- [5] A. Yamada, S.C. Chung, K. Hinomuka, *J. Electrochem. Soc.* 148 (2001) A224.
- [6] C. Delacourt, L. Laffont, R. Bouchet, C. Wurm, J.B. Leriche, M. Morcrette, J.M. Tarascon, C. Masquelier, *J. Electrochem. Soc.* 152 (2005) A913.
- [7] F. Zhou, M. Cococcioni, C.A. Marianetti, D. Morgan, G. Ceder, *Phys. Rev. B* 70 (2004) 235121.
- [8] T. Shiratsuchi, S. Okada, T. Doi, J. Yamaki, *Electrochim. Acta* 54 (2009) 3145.
- [9] S.M. Oh, S.W. Oh, C.S. Yoon, B. Scrosati, K. Amine, Y.K. Sun, *Adv. Funct. Mater.* 20 (2010) 3260.
- [10] Z. Bakenov, I. Taniguchi, *J. Power Sources* 195 (2010) 7445.
- [11] A.S. Aric  , P. Bruce, B. Scrosati, J.M. Tarascon, W. van Schalkwijk, *Nat. Mater.* 4 (2005) 366.
- [12] H. Fang, L. Li, G. Li, *Chem. Lett.* 36 (2007) 436.
- [13] S.M. Oha, S.W. Oha, S.T. Myungb, S.M. Leec, Y.K. Sun, *J. Alloys Compd.* 506 (2010) 372.
- [14] D. Wang, H. Buqa, M. Crouzet, G. Deghenghi, T. Drezen, I. Exnar, N. Kwon, J.H. Miners, L. Poletto, M. Grazel, *J. Power Sources* 189 (2009) 624.
- [15] Y. Wang, Y. Yang, Y. Yang, H. Shao, *Solid State Commun.* 150 (2010) 81.
- [16] T. Maxisch, F. Zhou, G. Ceder, *Phys. Rev. B* 73 (2006) 104301.
- [17] M.S. Islam, D.J. Driscoll, C.J. Fisher, P.R. Slater, *Chem. Mater.* 17 (2005) 5085.
- [18] C.J. Fisher, M.S. Islam, *J. Mater. Chem.* 18 (2008) 1209.
- [19] R. Amin, P. Balaya, J. Maier, *Electrochem Solid State Lett.* 10 (2007) A13.
- [20] D. Choi, D. Wang, I. Bae, J. Xiao, Z. Nie, W. Wang, V.V. Viswanathan, Y.J. Lee, J. Zhang, G.L. Graff, Z. Yang, J. Liu, *Nano Lett.* 10 (2010) 2799–2805.
- [21] L. Laffont, C. Delacourt, P. Gibot, M.Y. Wu, P. Kooyman, C. Masquelier, J.M. Tarascon, *Chem. Mater.* 18 (2006) 5520.
- [22] S.W. Kim, J. Kim, H. Gwon, K. Kang, *J. Electrochem. Soc.* 156 (2009) A635.